Microstructural stability and lattice misfit characterization of nimonic 263

LUO, Quanshun

Published version

LUO, Quanshun (2012). Microstructural stability and lattice misfit characterization of nimonic 263. In: Proceedings of the ASME 2012 Pressure Vessels & Piping Division Conference. ASME. (In Press)

Proceedings of the ASME 2012 Pressure Vessels & Piping Division Conference
PVP2012
July 15-19, 2012, Toronto, Ontario, Canada

PVP2012-78725

MICROSTRUCTURAL STABILITY AND LATTICE MISFIT CHARACTERISATIONS OF NIMONIC 263

Quanshun Luo
MERI, Sheffield Hallam University, Howard Street, Sheffield, S1 1WB, UK

Kuangnan Chi
Boiler Product Development, Doosan Power Systems, Porterfield Road, Renfrew, PA4 8DJ, UK

Shuxin Li
MERI, Sheffield Hallam University, Howard Street, Sheffield, S1 1WB, UK

Pete Barnard
Boiler Product Development, Doosan Power Systems, Porterfield Road, Renfrew, PA4 8DJ, UK

ABSTRACT

Nimonic 263 has been selected as a candidate header/piping material of advanced ultra-supercritical (A-USC) boilers for the next generation of fossil fuel power plant. Experimental assessments on the microstructural stability of this material are presented in this paper. Microstructural evolution has been quantified by high resolution field emission SEM and TEM. Electron diffraction and the combined XRD and Gaussian peak-fitting have been applied to investigate the coherency and lattice misfit between the gamma prime (γ') precipitates and the gamma (γ) matrix. The microstructure subjected to solution and hardening treatment consists of γ-matrix and a network of carbide precipitates along the grain boundaries. Large quantities of fine γ'-Ni_3(Ti,Al) precipitates were observed, with an average size of 17 nm and coherent with the matrix lattice. The overall misfit has been quantified to be 0.28%. After long term aging at 700 and 725 °C for various periods up to 20,000 hours, γ' was still the predominant precipitate and mostly coherent with the matrix. A few needle-shape η-Ni_3Ti intermetallic precipitates were found in the grain boundary regions. The γ' size has grown progressively to 78 nm, accompanied by the γ'-γ constrained misfit increasing to 0.50%. Moreover, the $M_{23}C_6$-type grain boundary carbides were found to have experienced morphological evolution, including the nucleation of Widmanstatten-type needles and their initial growth towards the matrix.

1. INTRODUCTION

The efficiency of coal fired power plant could be significantly improved by increasing the operating temperature and pressure. This would result in reduced CO_2 emissions per MW generated, and would also help offset the reduced efficiency caused by incorporating carbon capture. It is feasible to increase the cycle efficiency of coal fired power plant to approximately 50% by increasing the steam pressure to 350 bar and the final steam temperature to 700 °C [1-3]. In order to meet the requirement of higher resistance to creep rupture, corrosion and oxidation an upgrade in the materials used for the high temperature components from the currently used ferrous based alloys to nickel based superalloys is required. Nickel based superalloys are well known for their high temperature properties, however, unlike the applications in aerospace where the service time is typically a few thousands of hours, in thermal power generation the requirement is for service times of hundreds of thousand of hours. Consequently, a paramount issue is the stability of the microstructure of the candidate superalloys at the elevated temperatures [4, 5].

The aim of this investigation is to provide a comprehensive evaluation of the microstructure changes during long term aging of the nickel-based superalloy Nimonic 263, a candidate material for superheater headers.

Nimomic 263 is a wrought alloy with nominal chemical compositions, in weight percent (wt%), of Cr 20, Co 20, Mo 6, Ti 2, Al 0.5, Fe 1, C 0.06 and the balance Ni [6-8]. As a precipitation strengthening alloy, its heat treatments include a solution treatment at 1150 °C and a subsequent aging treatment at 800 °C, to form the standard hardened structure consisting of a γ-Ni based matrix containing fine coherent γ'-Ni_3(Ti, Al) intermetallic precipitates and preferential distribution of $M_{23}C_6$- and M_6C-type carbides along the γ-Ni grain boundaries (G.B.). The volume fraction, shape, size and distribution of the γ'-Ni_3(Ti, Al) precipitates depend on the Ti and Al contents and also on the aging treatment at elevated temperatures [4, 5, 8-16].

Nimonic 263 contains fine γ' precipitate particles due to its low Ti and Al content.

For many precipitation-hardening superalloys progressive structural evolution occurs at the service temperature, this plays an important role on the long-term performance. The growth of γ'precipitates at elevated temperatures follows a diffusion mechanism, with the relationship between precipitate size *d* and aging time *t* expressed by the so-called Lifshitz-Slyozov-Wagner (LSW) model, *i.e.* $d \propto t^3$ [4, 5, 8, 9, 11-13, 17]. Ref. [8] made thermodynamic calculation of the time-temperature-transformation (TTT) curves of the γ', η, $M_{23}C_6$ and M_6C precipitates in Nimonic 263 alloy, but pointed out that this method could not correctly predict the sluggish γ' → η transformation. In Inconel 617 alloy, needle-like $M_{23}C_6$ and M_6C carbides were observed after 704 °C aging for long periods up to 6.6×10^5 hours [4]. In another superalloy, Inconel 740, the γ' → η transformation took place when the alloy was aged at 750 °C and 816 °C for a series of aging times up to 2,500 hours [14 - 16]. Zhao *et al.* [8] reported that, for alloy 263, the γ' phase precipitated initially at 600 °C, became unstable at 800 - 900 °C and then completely dissolved into the γ matrix at 950°C.

In nickel based superalloys, the γ'/γ coherent misfit is defined by the equation $\delta = (a_{\gamma'}-a_{\gamma})/[0.5\cdot(a_{\gamma'}+ a_{\gamma})]$, where $a_{\gamma'}$ and a_{γ} stand for the lattice parameters of the γ'and γ phases respectively [9]. Several diffraction techniques have been developed for the misfit measurement, including X-ray diffraction (XRD) [18-21], neutron diffraction (ND) [22, 23], and convergent beam electron diffraction (CBED) in transmission electron microscopy (TEM) [18, 19, 24]. Although XRD is known for its high precision, the technique hasn't been used in misfit measurement because of the difficulty in deconvoluting overlapping γ'and γ diffraction peaks [18]. Consequently, a chemical extraction technique was developed to measure the unstrained lattice misfit using chemically extracted γ' particles [9, 15, 17, 18, 25]. Meanwhile, numerical peak deconvolution techniques, such as the Gaussian peak-fitting technique, have been developed to measure the constrained misfit of bulk samples [19, 23, 26]. However, only a few successful experiments have been reported on superalloys having low Ti and Al contents [20, 27]. To our knowledge, no precise measurement of γ/γ' misfit has been previously reported on age-hardened Nimonic 263 alloy.

In this paper, we report the microstructure evolution of wrought Nimonic 263 alloy after aging at 700 °C and 725 °C for up to 20,000 hours. A separate work on microstructure characterization of the same alloy has been reported elsewhere [28]. Along with extensive analyses of the microstructure changes by using high resolution scanning electron microscopy (SEM), TEM and selected area electron diffraction (SAD), the constrained γ'/γ lattice misfit has been measured precisely using a newly developed XRD and Gaussian numerical peak-fitting technique.

2. EXPERIMENTAL

The Nimonic 263 parent materials was manufactured by Special Metals as a 5-tonne cast, and then extruded by Wyman Gordon to produce pipe of nominal outside diameter 310mm and wall thickness 70mm. The material was solution treated at 1150 °C and water quenched (inside and outside) after extrusion, and supplied in this condition to Doosan Power Systems (DPS).

To explore the effect of service exposure, selected samples were exposed to a range of service simulation aging temperatures of 700 and 725°C, with aging times of 3,000 and 10,000 hours. An extended exposure time was carried out at 700°C for 20,000 hours. Table 1 lists the sample number, aging temperatures, exposure times, and the corresponding Larson-Miller parameter for these samples. The Larson-Miller parameter was defined to illustrate the temperature and time factors on creep of metallic alloys [4].

The samples for SEM and XRD characterization were mounted, ground and polished using an automatic grinding/polishing unit. The Fry's reagent was found to be effective in highlighting γ' precipitates.

A high resolution and analytical field emission SEM instrument, FEI Nova200 NanoSEM equipped with Oxford Inca energy dispersive X-ray (EDX) spectrometry, was employed in the microstructure characterization. TEM characterization was undertaken using a Philips CM20 instrument, with a tungsten filament and being operated at 200 kV. The TEM specimens were prepared by ion milling using a Gatan 691 Precision Ion Polishing System (PIPS) at low sputtering angles of ± 6° and ion energy of 3 – 5 keV.

A computer programmed Philips X-Pert X-ray diffractometer was employed for the X-ray diffraction work, using a Cu K_α radiation source (wavelength λ = 0.154056 nm for $K_{\alpha 1}$) working at 40 kV and 40 mA. All scans were acquired at the Bragg-Brentano mode in a range of diffraction angle, 2θ = 20 – 100°, to cover five diffraction peaks of the γ' and γ phases, namely the {111}, {200}, {220}, {311} and {222} planes. Other applied conditions included divergence and anti-scattering angles both at ¼ °, and step size of 0.0167° and 300 second/step. Gaussian approaching is known for the high precision in diffraction angle measurement [19, 20, 29]. In this work, we developed a MS-Excel based software based on the Gaussian function, to deconvolute the obtained γ/γ' diffractions. Each obtained original curve was processed by smoothening, $K_{\alpha 1}$ stripping, and background removing before the Gaussian peak-fitting. Both γ' and γ d-spacings were subsequently calculated after the Gaussian peak-fitting. The constrained lattice misfit was eventually determined from the lattice parameters a_γ and $a_{\gamma'}$.

3. RESULTS

3.1 SEM observations and EDX chemical analyses

Figure 1 is a collection of SEM images taken from differently aged samples. As the low magnification micrograph shown in Fig. 1a, the alloy has an equiaxed granular morphology. In all the aged samples, the matrix was found to contain a large quantity of nano-scale nodular shaped γ'-Ni_3(Ti, Al) precipitates without any needle-like η-Ni_3Ti, Fig. 1 b-d. Needle-like precipitates appeared predominantly at the G.B. regions after aging either at 700 °C for 20,000 hours (Fig. 1c) or at 725 °C for 10,000 hours (Fig. 1d).

According to previous research on similar superalloys [4, 8, 14-16], the needle-like precipitates could be carbides and or the η-Ni_3Ti intermetallic phase. In the SEM characterization, we employed the combined scanning back-scattered electron (BSE) imaging and EDX spectroscopy to identify the needle-like precipitates. The analysis was conducted on the ion beam milled TEM samples in order to avoid artificial contaminants arising from sample polishing. In general, the aged superalloy contained three types of phases, namely the metallic matrix, the Ti- and Al-rich intermetallics γ'-Ni_3(Ti, Al) and η-Ni_3Ti, and the Cr-Mo carbides. The different mass densities of these phases should result in different levels of BSE contrast, i.e. from the bright γ-Ni matrix, to the intermediate contrast of the intermetallics and the dark contrast of the carbides. This BSE capability has been verified by the different contrast between the γ-Ni matrix and the γ'-Ni_3(Ti, Al) precipitates, Fig. 1. On the other hand, although the spatial resolution of SEM-EDX spectroscopic analysis is not sufficiently high to obtain any absolute spectrum from a nano-scale object due to the relatively larger sample thickness and the electron beam interaction volume, we could not ignore the possibility of detecting the difference of the chemical compositions between the different structural components. The combined SEM-BSE and EDX analysis was firstly applied on the 725 °C and 10,000 hour aged alloy. Figure 2 is a high-magnification BSE image showing the G.B. region and a few selected EDX spectra acquired at different objects. Typical EDX results are shown in Table 2. On the image, both the left and right sides shows the matrix structure containing the γ-Ni matrix and γ'-Ni_3(Ti, Al) nodular precipitates. Note that the latter are distinguished from the former by their relatively dark BSE contrast. The middle part of the image shows the G.B. region in which several needles (labelled '1' to '3') locate adjacent to the blocky and rectangular grains (labelled '5' and '6' respectively). The needles labelled '1' and '2' show similar contrast to the γ' precipitates. EDX spectra acquired in the two objects show slightly higher Ti and Ni contents than the matrix region. These results suggest that the needles are likely intermetallic phase in the η-Ni_3Ti type. The blocky grains, like the one labelled '5', are Cr-Mo carbides according to the dark BSE contrast and the higher Cr, Mo and C contents than the matrix. Interestingly, some of the needle- and rod-like precipitates are more like Cr-Mo carbide phase than the η-Ni_3Ti intermetallic phase according to their dark BSE contrast. In addition, the grain boundary region adjacent to the η-Ni_3Ti needles, labelled '4', was found to contain higher Ti than other area, which might be related to the nucleation of the η-Ni_3Ti.

The combined SEM-BSE and EDX analysis was also applied on the sample aged at 700 °C for 20,000 hours. Figure 3 shows a BSE image of the sample. Table 3 shows the normalised EDX quantification of Ni, Co, Cr, Mo and Ti contents of typical areas. Several needle-like precipitates can be found at close proximity of the G.B. region. Needles labelled '1' and '2' have grown penetrating into the matrix, whereas rods '3' and '4' both lay along the grain boundary. Needles '1' and '2' are likely η-Ni_3Ti according to the similar BSE contrast to the adjacent matrix and the lower Cr and slightly higher Ti contents than the matrix. Rods '3' and '4' are more likely Cr-Mo carbides. EDX analysis confirmed that the dark-contrast particles along the grain boundary were Cr-Mo carbides. In addition, two similar Cr-Mo carbide precipitates were found inside the matrix grain on the right hand side.

3.2 TEM observations and SAD analysis

Figure 4 shows TEM observations of the alloy after solution treated at 1150 °C and aged 800 °C. Figure 4a is a BF image showing the G.B. region between two matrix grains. Most of the carbide precipitates in the G.B. region exhibit equiaxed granular morphology. The matrix grains are full of fine nodular-shape γ'-Ni_3(Ti,Al) precipitates. The size of the γ'-Ni_3(Ti,Al) precipitates has been determined to be 17 ± 5 nm, out of 120 measurements. The SAD pattern shown in Fig. 4b is a [112]-axis reciprocal lattice of the face-centre-cubic (fcc) γ and γ' phases. The existence of the γ' phase is demonstrated by the presence of the weak superlattice diffractions in the {110} and {210} planes. Note that, the diffraction spots of the γ' precipitates are well aligned to the diffraction of the γ matrix, suggestive of well-defined coherency between γ and γ', whereas further precise XRD measurement of the coherency misfit will be discussed later.

Figure 5 shows a low magnification TEM BF image of the alloy aged at 700 °C for 20,000 hours. Central area of the image shows the grain boundary between the upper and lower matrix grains. Unlike the carbides of the as-hardened alloy shown in Fig. 4a, the carbide precipitates exhibit various morphologies, *e.g.* needles, rods, and well-defined rectangles. In Fig. 6, the equiaxed carbide grains in the grain boundary served as nucleation sites of Widmanstatten-type structure. These observations give more details of the morphological changes, being consistent with the SEM observations shown in Fig. 2-4. The matrix grains in the upper part exhibit strong diffraction contrast and show the fine γ' precipitates. More interestingly, the matrix grain in the lower part was in such an orientation with respect to the electron beam that the γ' precipitates were contrasted to the surrounding γ matrix predominantly by the mass difference owing to the minimised diffraction contrast. In

such imaging condition, the lighter γ' phase gave rise to less inelastic electron scattering and hence showed brighter contrast. Consequently the size of γ' precipitates can be measured precisely. The γ' precipitate size was determined to be 78 ± 15 nm, out of 120 measurements. Figure 7a is a BF image of the matrix area. The Moire patterns indicate the locations of some precipitates. The change in the matrix contrast indicates coherent lattice straining arising from the γ/γ' misfit. Figure 7b is a SAD pattern of the imaged area, in which distinct diffraction spots of the ordered γ' phase are well aligned to the strong spots of the γ phase. Similar to the diffraction characteristic shown in Fig. 4b, the diffraction analysis suggests that the γ' precipitates still remained coherent to the γ matrix.

3.3 XRD measurement of the γ/γ' misfits

XRD scans have been undertaken on most of aged samples. A typical scan is shown in Fig. 8a, in which the diffraction peaks, i.e. (111), (200), (220), (311) and (222) following a sequence of increasing 2θ angle, exhibit various intensities. Gaussian numerical approaching has been applied on all the obtained diffraction peaks to separate the γ and γ' diffractions. An example of the peak separation is shown in Fig. 8b. It shows that, the original diffraction has been separated as two sub-peaks, whereas the major one was from the γ phase and the minor one from the γ' phase. Table 4 provides the results of one sample as an example of the measurements. The constrained lattice misfits measured from the five diffraction peaks show a statistic value of (0.28 ± 0.10)%. Table 5 lists a summary of all the measurements. When the alloy was aged at 700 °C for an increasing period from 3,000 to 20,000 hours, the misfit increased from 0.39% to 0.50%, suggesting a progressive increase of the misfit with the γ' coarsening. The measurements also show that aging at higher temperature resulted in faster increase of the lattice misfit, i.e. comparing the values 0.45% (at 725 °C) and 0.39% (at 700 °C) of the 10,000 hour aged alloys.

4. DISCUSSION

Nimonic 263 is a precipitate-strengthened superalloy, in which both the carbide and intermetallic precipitates are designed to play a key role in the high temperature strengthening. This investigation has demonstrated that, the alloy exhibited good thermal stability in the long-term aging process although certain important structural evolutions took place both in the γ'-Ni_3(Ti,Al) intermetallic precipitates and in the grain boundary carbides.

The γ'-Ni_3(Ti,Al) precipitates have survived as the primary hardening phase of the matrix without transforming to the needle-like η-Ni_3Ti. And most of the γ'-Ni_3(Ti,Al) precipitates still remained coherent to the γ-Ni matrix. Moreover, the γ'-Ni_3(Ti,Al) precipitates have grown from their original size of 17 nm to 78 nm after the long-term aging, accompanying an increase of the constrained γ'/γ lattice misfit from 0.28% to 0.50%.

For precipitate-strengthening superalloys, the γ'→η transformation is thought to trigger embrittlement. Such a transformation has been reported in another precipitate-strengthening superalloy, the Inconel 740 [5, 16, 30]. For Nimonic 263, both thermodynamic calculation and experimental studies have found the formation of η-Ni_3Ti needles at aging temperatures higher than 750 °C [8]. The current research confirms that, γ' was still the dominant strengthening phase after long-term aging behaviour at 700 °C and 725 °C. Moreover, the progressive growth of the γ' size was dominated by a diffusion controlled kinetics, which is consistent to previous reports in Nimonic 263 and other superalloys [4, 5, 8, 9, 11-13, 31]. The excellent thermal stability promises a good precipitate-strengthening capacity for long-term applications.

The constrained γ'/γ lattice misfit of Nimonic 263 has been experimentally measured here by using the combined X-ray diffraction and Gaussian peak-fitting techniques. The misfit values, between 0.28% and 0.50%, are within the similar range of other nickel based superalloys [13, 18, 20, 22, 26]. These data confirm the feasibility of XRD technique in the challenging misfit measurement of nickel superalloys having low Ti and Al contents [20, 27]. The small value of 0.28% in the as-hardened alloy and the subsequent increase to 0.40% – 0.50% in the long-term aged samples indicate the dependence of the constrained misfit on the γ' particle size. In bulk samples, the constrained misfit can be considered as a sum of the un-strained misfit, determined from free-standing γ' particles and a γ'-free matrix, and the elastic misfit arising from the elastic strain field to match a coherent γ'/γ interface [17, 30]. Whereas the unstrained misfit is a function of the chemical compositions of γ' and γ components, the elastic misfit is directly related to the elastic strain arising from the coherent γ'/γ interface. For the as-hardened sample, the small volume of each γ' particle was subjected to a high scale of elastic strain and consequently led to a smaller constrained misfit value. When the γ' size became bigger in the aged samples, the elastic straining should be less pronounced, so that the constrained misfit was more dominated by the intrinsic lattice property of the γ' phase, i.e. having its value closer to the unstrained misfit measured from free-standing γ' particles. A similar relationship has been recently reported in another nickel base superalloy [26].

Fitting current results into a lattice parameter-aging time curve, Fig. 9, shows that for specimens aged at 700°C, compared with lattice parameters of solution and hardened state, both γ' and γ had reduced lattice parameters at the early stage of aging (up to 3000 hours) and then both increased their values with further increasing of the aging time. This is consistent with the previous published data [17].The initial reduction of γ and γ' lattice parameter may be due to further γ' precipitation, and the long range ordering effect occurring during aging. With the further

increasing of aging time (>3000 hours) at 700°C, the enlargement of γ' lattice is obvious, while the lattice parameter of γ almost remained the same after its initial increase, these perhaps mostly were attributable to the long range ordering effect. Moreover, results at 725°C indicate that there is more reduction in lattice parameter for both γ and γ' at the aging time of 10,000 hours, compared with results at 700°C.

The G.B. carbide precipitates exhibited complex morphology of various shapes after the long-term aging, Fig. 5-7. This indicates that the equiaxed granular carbides precipitated in the as-hardened alloy, i.e. after only a few hours of aging at 800 °C, still had further potential to lower the free energy by progressive change in the morphology. During long term aging at 700 °C and 725 °C, evolution of the grain boundary precipitates took place gradually to form various carbide shapes from rectangles, rods, to needles. In particular, an interesting phenomenon has been the formation of rod- and needle-like phases, as well as the initial Widmanstatten-type structure. Some of the rods and needles are Cr-Mo carbides, which are similar to those observed in a similar nickel based superalloy IN617 after long term aging (704 °C and 65,600 hours) [4]. Meanwhile, the formation of η-Ni_3Ti intermetallic needles is consistent to those reported in literature [14-16, 30]. Nevertheless, the needle-like precipitates are still in their initial form, i.e. distributed only along the grain boundaries, therefore should not result in a significant impact on mechanical properties.

Moreover, it was noticed that, the nucleation of carbide needles was based on the surface of existing $M_{23}C_6$ phases, whereas the intermetallic needles were found to originate at a localised Ti-rich region. However, further work is still needed to fully understand the kinetics of the needle phase precipitation.

5. CONCLUSIONS

The structural stability of Nimonic 263 superalloy exposed to long-term aging at elevated temperatures has been studied. Following conclusions can be made:

1) The sample after solution treatment and age hardening exhibited microstructure consisting of equiaxial γ grains, with homogeneous γ' precipitates, and a network of blocky $M_{23}C_6$-type precipitates along G.B. The γ' precipitates showed an average size of 17 nm, being coherent to the matrix with a low constrained lattice misfit of 0.28%.
2) After being aged at 700 and 725 °C for various periods up to 20,000 hours, γ' was still the predominant precipitate phase and mostly coherent to the matrix. Its average size has grown up to 78 nm, accompanied by an increase of the constrained lattice misfit to 0.50%.
3) After aging, the $M_{23}C_6$-type carbides at the grain boundaries experienced an evolution in morphology, with the formation of rod- and needle-like precipitates as well as initial growth of Widmanstatten-type structure. These newly formed precipitates included both $M_{23}C_6$-type carbides and η-Ni_3Ti intermetallics.
4) Above all, the structure characterisation on Nimonic 263 has demonstrated decent thermal stability at the tested temperatures.

REFERENCES

[1] P. M. Barnard, L. W. Buchanan and M. Barrie, Material developments for supercritical boilers and pipework – bridging the gap? Materials for Advanced Power Engineering, Liege, (2010).

[2] I. G. Wright, P. J. Maziasz, F. V. Ellis, T. B. Gibbons, D. A. Woodford, Materials issues for turbines for operation in ultra-supercritical steam, Oak Ridge NL report: http://www.ms.ornl.gov/CST/pdf/IGW-0417.pdf.

[3] G. R. Holcomb, D. Hsu, Steam turbine materials and corrosion, presented in 22nd annual conference on fossil energy materials, Pittsburgh, USA, July 8-10, (2008).

[4] Q. Wu, H. Song, R.W. Swindeman, J.P. Shingledecker, V.K. Vasudevan, Microstructure of long-term aged IN617 Bi-based superalloy, Metall. Mater. Trans 39A, (2008), 2569-2585.

[5] S. Zhao, X. Xie, G. D. Smith, S. J. Patel, Microstructural stability and mechanical properties of a new nickel based superalloy, Mater. Sci. Eng. A355 (2003) 96 – 105.

[6] V. Ratna, D. S. Sarma, Influence of thermal fatigue on the microstructure of a Ni based superalloy, Script. Metall. Mater. 29 (1993) 467 – 472.

[7] P. N. Singh, V. Singh, Influence of aging treatment on work hardening behaviour of a Ni-based superalloy, Script. Mater. 34, (1996), 1861-1865.

[8] J. C. Zhao, V. Ravikumar, A. M. Beltran, Phase precipitation and phase stability in Nimonic 263, Metall. Mater. Trans. 32A, (2001), 1271-1282.

[9] E. Nembach, G. Neite, Precipitation hardening of superalloys by ordered γ'-particles, Progress in Mater. Sci. 29, (1985), 177-319.

[10] A Nitz, E Nembach, Critical resolved shear stress anomalies of the $L1_2$-long-range ordered gamma' phase of the superalloy Nimonic 105, Mater. Sci. Eng. A263 (1999) 15-22.

[11] A Baldan, Review: Progress in Ostwald ripening theories and their applications to the gamma' precipitates in nickel based superalloys, J. Mater.

Sci. 37 (2002) 2379 – 2405.

[12] A Takahashi, M Kawanabe, NM Ghoniem, Gamma precipitates strengthening in nickel based superalloys, Philosophical Magzine 90 (2010) 3767 – 3786.

[13] R. A. Ricks, A. J. Porter, R. C. Ecob, The growth of γ'precipitates in nickel-base superalloys, Acta Metall. 31 (1983) 43-53.

[14] S. Zhao, X. Xie, G. D. Smith, SJ Patel, Research and improvement on structure stability and corrosion resistance of nickel based superalloy Inconel alloy 740, Mater. Design 27 (2006) 1120 – 1127.

[15] S. Zhao, X. Xie, G. D. Smith, S. J. Patel, Gamma prime coarsening and age-hardening behaviours in a new nickel based superalloy, Mater. Lett. 58 (2004) 1784 – 1787.

[16] N. D. Evans, P. J. Maziasz, R. W. Swindeman, G. D. Smith, Microstructure and phase stability in Inconel alloy 740 during creep, Scripta Mater. 51 (2004) 503 – 507.

[17] J. Tiley, G.B. Viswanathan, J.Y. Hwang, A. shiveley, R. Banerjee, Evaluation of gamma prime volume fractions and lattice misfits in a nickel base superalloy using the external standard X-ray diffraction method Mater. Sci. Eng. A528 (2010) 32 – 36.

[18] R. C. Ecob, R. A. Ricks, A. J. Porter, The measurement of precipitate/matrix lattice mismatch in Nickel based superalloys, Scrip. Metall. 16 (1982) 1085-1090.

[19] D. F. Lahrman, R. D. Field, R. Darolia, H. L. Fraser, Investigation of techniques for measuring lattice mismatch in a rhenium containing nickel based superalloy, Acta Metall. 36 (1988) 1309-1320.

[20] D. Mukherji, R. Gilles, B. Barbier, D. Del. Genovese, B. Hasse, P. Strunz, T. Wroblewski, H. Fuess, J. Rösler, Lattice misfit measurement in Inconel 706 containing coherent γ' and γ" precipitates, Scrip. Mater. 48 (2003) 333–339.

[21] S. K. Rai, A. Kumar, V. Shankar, T. Jayakumar, K. B. S. Rao, B. Raj, Characterization of microstructures in Inconel 625 using X-ray diffraction broadening and lattice parameter measurements, Scrip. Mater. 51 (2004) 59-63.

[22] M. Hoelzel, D. D. Genovese, R. Gilles, D. Mukherji, D. M. Toebbens, J. Roesler, H. Fuess, Phase analysis and lattice mismatches in superalloys DT706 and Inconel 706, Physica B: Physics of Condensed Matter 385, (2006), 594-596.

[23] R. Gilles, D. Mukherji, M. Hoelzel, P. Strunz, D. M. Toebbens, B. Barbier, Neutron and X-ray diffraction measurements on micro- and nano-sized precipitates embedded in a Ni-based superalloy and after their extraction from the alloy, Acta Mater. 54 (2006) 1307-1316.

[24] J. Li, R. P. Wahi, Investigation of γ/γ' lattice mismatch in the polycrystalline nickel-based superalloy IN738LC: Influence of heat treatment and creep deformation, Acta Metall. Mater. 43, (1995), 507-517.

[25] K. Kusabiraki, H. Komatsu, S. Ikeuchi, Lattice constants and compositions of the metastable Ni_3Nb phase precipitated in a Ni-15Cr-9Fe-6Nb alloy, Metall. Mater. Trans. A29, (1998), 1169-1174.

[26] S. Tian, M. Wang, H. Yu, X. Yu, T. Li, B. Qian, Influence of element Re on lattice misfits and stress rupture properties of single crystal nickel-based superalloys, Mater. Sci. Eng. A 527 (2010) 4458-4465.

[27] A. Sarkar, P. Mukherjee, P. Barat, T. Jayakumar, S. Mahadevan, S.K. Rai, Lattice misfit measurement in Inconel 625 by X-ray diffraction technique, Inter. J. Modern Phys B 22, (2008), 3977-3985.

[28] S. A Smith, G. D. West, K. Chi, W. Gamble and R. C. Thomson, Microstructural evolution in Nimonic 263 for high temperature power plants, Proc. of 6th Int. Conf. on Advances in Materials Technology for Fossil Power Plants, 31 August - 3 September (2010), Santa Fe, NM, USA.

[29] B. D. Cullity, S.R. Stock, Elements of X-ray Diffraction, 3rd edition, Prentice Hall, Upper Saddle River, NJ, (2001), p. 435.

[30] S. Zhao, X. Xie, Properties and microstructure after long-term aging at different temperatures for a new nickel based superalloy, Acta Metall. Sinica 39, (2003), 399-404.

[31] J Tiley, GB Viswanathan, R Srinivasan, R Banerjee, DM Dimiduk, HL Fraser, Coarsening kinetics of gamma' precipitates in the commercial nickel based superalloy Rene 88 DT, Acta Mater. 57 (2009) 2538 – 2549.

ANNEX TABLES AND FIGURES

Table 1 Test conditions of Nimonic 263 samples, associated with Larson-Miller parameters.

No.	Temperature (T, °C)	Time (t, hour)	T(20+log t)
1	As-hardened	-	-
2	700	3,000	22843
3	700	10,000	23352
4	700	20,000	23644
5	725	3,000	23430
6	725	10,000	23952

Table 2 Normalised chemical composition (at%) of the labelled structural constituents in Fig. 2.

Locations	**C**	**Ni**	**Co**	**Cr**	**Mo**	**Ti**	**Al**	**Mn**	**Fe**
matrix	11.2	44.4	17.3	20.0	2.8	1.7	1.4	0.6	0.6
1 - needle	15.7	46.3	14.8	15.1	2.3	3.5	1.4	0.5	0.4
2 - needle	13.1	45.0	16.6	17.9	2.9	2.2	1.4	0.5	0.5
3 - needle	17.8	42.5	16.4	17.2	2.1	1.7	1.3	0.4	0.5
4 - G.B. grey	13.5	46.4	14.0	17.2	2.3	4.1	1.4	0.8	0.4
5 - Cr-Mo-C	22.1	29.8	11.2	30.0	3.5	1.7	0.9	0.5	0.3
6 - G.B. black	14.4	41.8	16.0	21.3	2.7	1.8	1.3	0.4	0.4

Table 3 Normalised chemical composition (at%) of the labelled structural constituents in Fig. 3.

Locations	**Ni**	**Co**	**Cr**	**Mo**	**Ti**
matrix	52.1	18.4	16.3	6.6	2.1
1 - needle	51.2	17.8	16.5	6.0	2.4
2 - needle	52.2	16.8	14.7	6.0	2.7
3 - rod	38.7	13.5	27.5	7.8	2.0
4 – rod	46.4	16.3	20.8	7.7	1.7
G.B.	34.8	12.3	33.7	8.1	2.4
G.B.	25.6	11.3	45.4	9.2	1.3
G.B.	44.2	14.7	21.3	6.1	3.8
G.B.	34.6	10.8	34.5	8.9	2.0

Table 4 Quantification of the Gaussian-fitted XRD results of the solution-hardening treated alloy.

(hkl)	2θ (degree)		I (count)		$I_{\gamma'}$ (%)	d, nm (nm)		a_0, nm (nm)		Misfit (%)
	γ	γ'	γ	γ'		γ	γ'	γ	γ'	
(111)	43.72	43.58	74242	13636	15.5	0.2069	0.2075	0.3584	0.3594	0.29
(200)	50.85	50.62	11363	2572	18.5	0.1794	0.1802	0.3589	0.3604	0.41
(220)	74.90	74.78	25757	9090	26.1	0.1267	0.1269	0.3583	0.3588	0.13
(311)	90.91	90.58	6212	1666	21.1	0.1081	0.1084	0.3585	0.3595	0.28
(222)	96.26	95.92	5151	755	12.8	0.1034	0.1037	0.3583	0.3593	0.27

Table 5 Lattice parameters and constrained lattice misfit of the γ and γ' phases of the investigated samples.

No.	Aging treatment	a_0-γ (nm)	a_0-γ' (nm)	Misfit (%)
1	As-hardened	0.3585	0.3595	0.28 ± 0.10
2	700 ^{0}C / 3,000 hours	0.3580	0.3593	0.36 ± 0.08
3	700 ^{0}C / 10,000 hours	0.3581	0.3595	0.39 ± 0.10
4	700 ^{0}C / 20,000 hours	0.3582	0.3600	0.50 ± 0.20
6	725 ^{0}C / 10,000 hours	0.3578	0.3594	0.45 ± 0.08

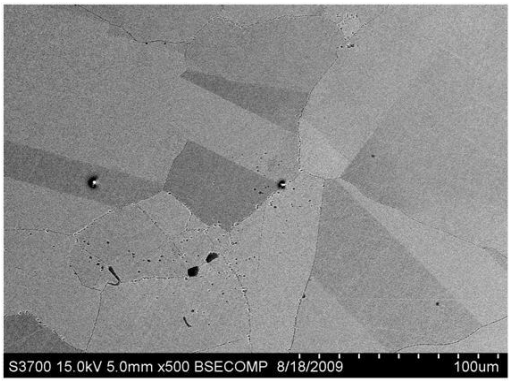

(a)

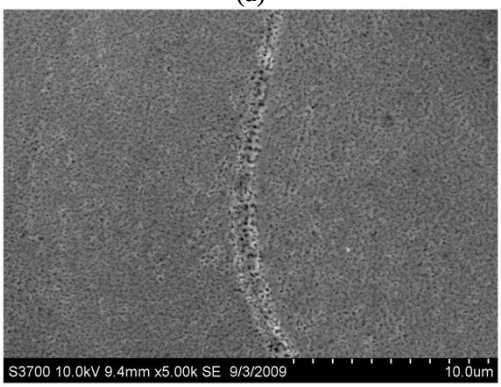

(b)

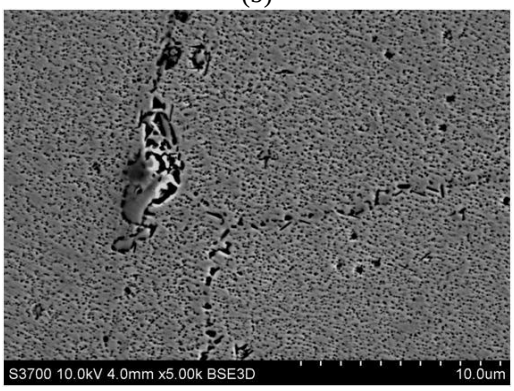

(c)

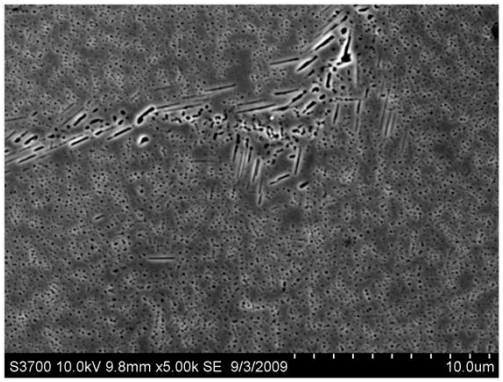

(d)

Figure 1 SEM images showing the microstructure of the aged samples. (a) Typical equiaxed granular morphology at low magnification; (b) 700 °C – 10kh aged alloy; (c) 700 °C – 20kh aged alloy; (d) 725 °C – 10kh aged alloy.

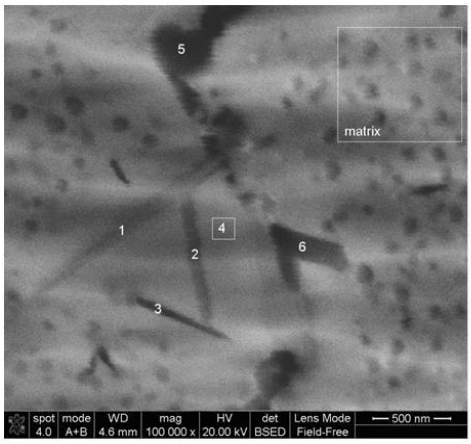

(a)

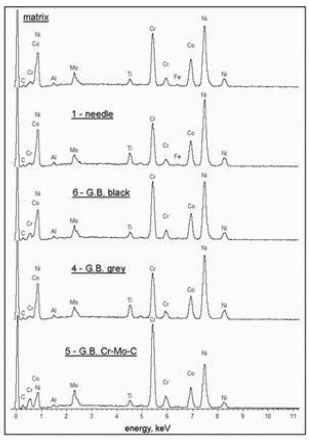

(b)

Figure 2 (a) A high magnification back-scattered SEM image showing various structural constituents in the grain boundary region of the 725 °C and 10kh aged alloy; (b) EDX spectra acquired at typical regions as labelled in the BSE image.

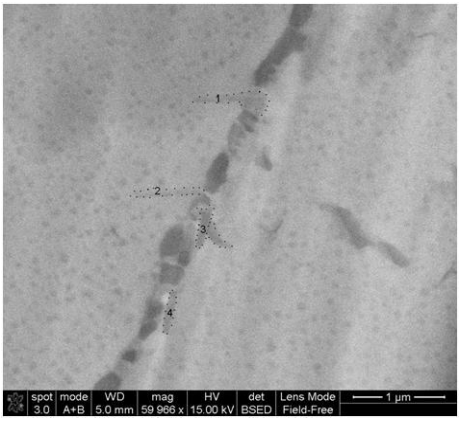

Figure 3 A back-scattered SEM image of the 700 °C 20kh aged alloy showing needle- and rod-like precipitates in the grain boundary region, labelled '1 – 4' and highlighted with black dots along the needle boundaries.

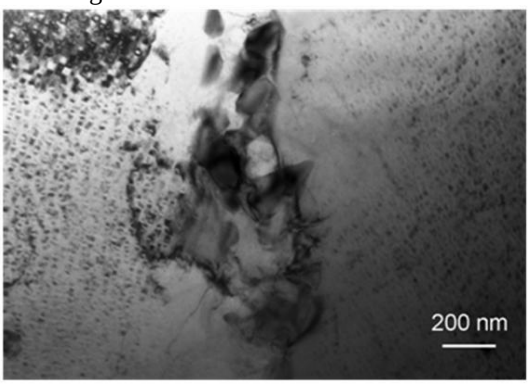

(a)

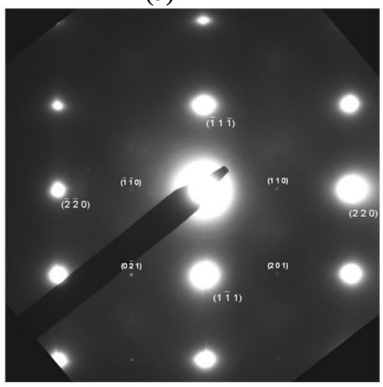

(b)

Figure 4 TEM BF micrographs and SAD analysis of the 1150°C-solutioning and 800 °C-aged alloy: (a) a BF image showing overall view of the matrix and grain boundary; (b) a SAD patterns of the matrix.

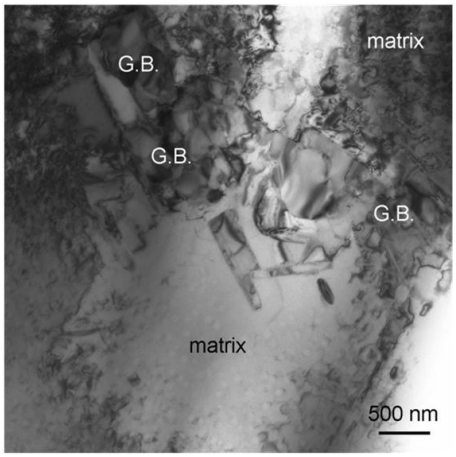

Figure 5 A TEM BF image of the 700 °C-20kh aged alloy, showing an overview of the grain boundary and matrix morphology.

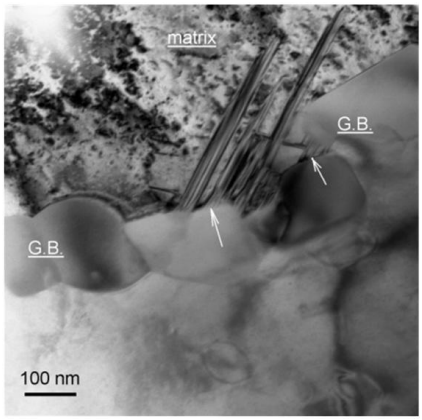

Figure 6 A TEM BF image of the 700 °C-20kh aged alloy, showing initial growth of Widmanstatten-type precipitates from blocky carbide grains of the matrix grain boundary. The arrows indicate the locations of the Widmanstatten-type phase nucleation.

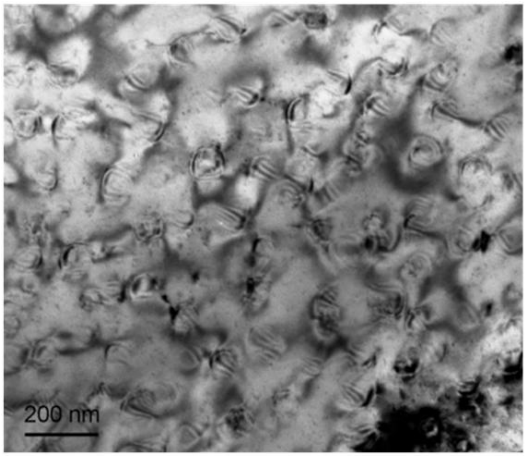

(a)

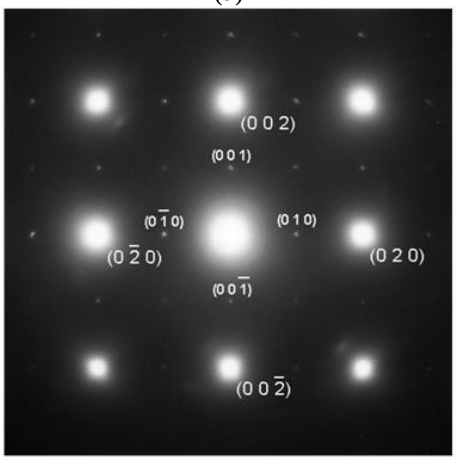

(b)

Figure 7 (a) A BF image and (b) the associated SAD pattern taken from the matrix region of the 700 °C-20kh aged alloy.

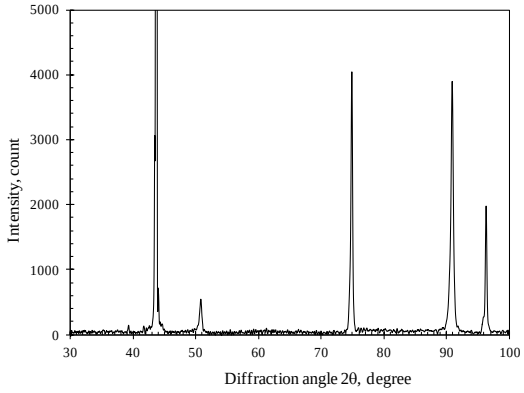

(a)

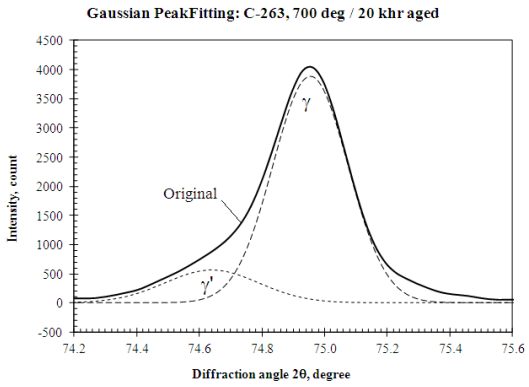

(b)

Figure 8 XRD measurement of the γ/γ' constrained lattice misfit: (a) an XRD curve acquired from the 700 °C-20kh aged alloy showing the (111), (200), (220), (311) and (222) diffraction peaks; (b) an example chart showing the Gaussian peak-fitting.

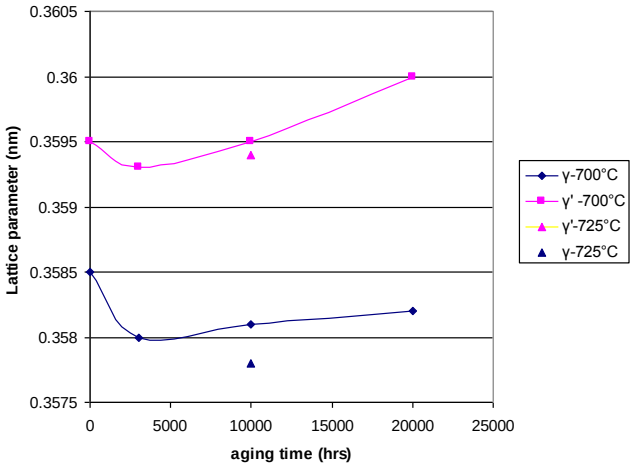

Figure 9 Lattice parameters for γ and γ' as a function of aging time, at 700 and 725°C.